

A thermomechanical finite element model and its comparison to inherent strain method for powder-bed fusion process

Can Bayraktar^{a,b}, Eralp Demir^{c,*}

^a*Faculty of Engineering and Natural Sciences, Sabanci University, Tuzla, Istanbul, Turkey*

^b*Integrated Manufacturing Tech. Research and App. Center, Sabanci University, Tuzla, Istanbul, Turkey*

^c*Department of Mechanical Engineering, University of Bristol, Bristol, BS8 1TR, UK.*

Abstract

In this study, a thermomechanical model is developed to predict the melt-pool dimensions and residual stresses for laser powder bed fusion process. Inherent strain method is also used to predict residual stresses by using only the thermal solution that is free the complexities involved with the mechanical solution. A unique approach is developed to define the surface heat losses as volumetric heat losses in order to avoid the definition of traction-free surfaces and their re-definition after layer deposition. The thermal process simulations predicts melt-pool dimensions of experimental cross-sections of single tracks within approximately 10% agreement. The thermomechanical process model is used to forecast the effect of process parameters on the melt-pool dimensions and residual stresses. The inherent strain method reproduces the residual stresses within 15% accuracy, approximately six times faster in comparison to the thermomechanical model, and free of any convergence issues related with the displacement field solution.

Keywords:

powder bed fusion, thermomechanical process model, FEM, inherent strain method

Nomenclature

α thermal expansion coefficient

β rigidity constraint in ISM

$\epsilon, \Delta\epsilon$ total strain and increment

ϵ_e elastic strain

$\epsilon_p, \Delta\epsilon_p$ plastic strain and increment

$\epsilon_T, \Delta\epsilon_T$ thermal strain and increment

σ stress

*Corresponding author

Email address: eralp.demir@bristol.ac.uk (Eralp Demir)

30	$\boldsymbol{\sigma}^{tr'}$	trial deviatoric stress
31	$\boldsymbol{\sigma}^{tr}$	trial stress
32	Δd	hatch spacing
33	Δh	layer thickness
34	ΔH_{ν}^*	effective enthalpy of metal vapor
35	Δp	plastic strain increment
36	Δt_{recoat}	time step at the recoating time interval
37	Δt_{scan}	time step at the scan time interval
38	\dot{Q}	heat input of the moving heat source
39	\dot{q}_{conv}	convective heat loss from surfaces
40	\dot{q}_{eff}	effective surface heat loss
41	\dot{q}_{eva}	evaporative heat loss from surfaces
42	\dot{q}_{rad}	radiative heat loss from surfaces
43	ϵ_{IS}	scalar inherent strain
44	η	efficiency factor / absorptivity
45	$\hat{\mathbf{T}}_{\mathbf{t}}$	nodal temperatures at former time increment
46	$\hat{\mathbf{T}}$	nodal temperatures
47	$\hat{\mathbf{u}}$	node displacements
48	\mathbf{B}	strain-displacement mapping
49	\mathbf{C}	elasticity matrix
50	\mathbf{E}	inherent strain
51	\mathbf{k}	conductivity matrix
52	\mathbf{n}	area normal of a surface
53	$\mathbf{N}, \mathbf{N}_{\mathbf{s}}$	volume and surface interpolation functions
54	\mathbf{n}_p	plastic flow direction
55	$\mathbf{q}, \mathbf{q}_{\mathbf{s}}$	volumetric and surface heat flux
56	\mathbf{R}	rotation matrix

57	\mathbf{S}	inherent stress
58	\mathbf{u}	displacements
59	\mathbf{x}_s	surface position vector
60	\mathbf{x}	position vector
61	$\nabla \mathbf{N}$	interpolation function derivatives
62	ω	material state indicator, solid volume fraction at mushy state
63	ψ	yield function
64	ρ	mass density
65	σ_y	yield stress
66	σ_{VM}	equivalent Von Mises stress
67	θ	scan direction with respect to sample x-axis
68	ε	emissivity
69	φ	solid volume fraction of powder state
70	$\hat{\boldsymbol{\sigma}}$	node values of stress
71	A, A_s, C	constants used in inherent strain & stress calculation
72	a, f_0	scaling factors to find powder conductivity
73	$A^{(H)}$	areal fraction of voids in powder state
74	C_p	specific heat
75	d_x, d_y, d_z	distances from the heat source along x, y, and z directions
76	E	Young's modulus
77	h	convection coefficient
78	$k^{(s)}, k^{(Ar)}, k^{(\varphi)}$	conductivity of solid, Argon gas, and powder, respectively.
79	K_B	Boltzmann constant
80	k_x, k_y, k_z	thermal conductivity constants x, y, and z directions
81	L	characteristic element size along scan direction
82	M	molar mass of metal vapor
83	P	laser power

84	P_0	ambient pressure
85	R	Universal gas constant
86	r	effective radius of the heat source
87	r_x, r_y, r_z	heat source radii
88	S	surface of the domain
89	T	temperature
90	t	time
91	T_0	ambient temperature
92	T_2, T_1	upper and lower limit temperature for ISM
93	T_ν	boiling temperature
94	T_s	surface temperature
95	V	volume of the domain
96	v	scan speed

97 1. Introduction

98 Additive manufacturing (AM) has been referred to as the manufacturing method of the
99 future. AM has become a great alternative to conventional manufacturing processes in
100 various industries because of its numerous advantages, such as process automation, reduc-
101 tion of multi-stage manufacturing processes, elimination of tooling, consumables, and waste
102 products [1]. In addition, AM makes it possible to produce highly complex geometries and
103 lightweight structures to significantly improve the design performance. Currently, AM has
104 found wide use in high-end applications in aerospace and biomedical industries. However,
105 still the applications of AM in critical industries require a better understanding of the effect
106 of process parameters on the product quality.

107 The laser powder bed fusion (LPBF) process is an AM process for manufacturing parts
108 with fine precision. In the LPBF process, a laser is used as the heat source to melt the metal
109 powder particles selectively and to solidify them by cooling in a layer-by-layer manufacturing
110 [2]. After selective melting of each layer over a powder substrate, a new layer of powder
111 material is added on top of the former layer, and the same procedure continues until the
112 part geometry is complete. Although this process has great advantages, AM suffers from the
113 formation of defects, residual stresses during deposition, and distortions that cause deviations
114 from the desired geometry [3]. High thermal gradients during the LPBF process lead to the
115 formation of tensile stresses that adversely affect the mechanical performance by promoting
116 crack initiation or formation. Residual stresses also cause loss of dimensional accuracy owing
117 to the distortions. Accordingly, the process parameters need to be optimized to ascertain

the penetration of melt zones with each other and integration of each layers for different materials [4].

Experimental trial-error methods to correlate the process parameters with the quality of product for LPBF process is a tedious and costly task because of the high machine costs involved with the AM process [5]. Therefore, researchers have turned their attention on developing efficient numerical methods to simulate the PBF process instead [6], which is consistent with the current research trends related to the digitization and digital twinning of AM processes. Process simulations have been used to unravel: the link between process parameters and the structural properties [7], anisotropic microstructure evolution [8], melt-pool kinetics [9], defect formation mechanisms [10], phase transformations [11], and solidification microstructure [12].

Thermomechanical finite element (FE) process simulations have been extensively used to determine the temperatures and displacements and to compute the melt-pool size and residual stresses after the AM process [13, 14]. Beuth et al. investigated the prediction of distortion after deposition as a pioneering study in this field [15]. The modeling of AM processes includes specific FE procedures such as element birth/death methods [16], ghost elements [17], and hybrid element activation methods [18, 19]. All of these process models were utilized in conjunction with temperature-dependent material properties [20, 21].

Melt-pool characteristics such as dimensions and geometry have a considerable effect on the overall part quality, hence it has been the subject of many studies [22]. Andreotta et al. developed a thermal model to predict melt-pool dimensions for various process parameter combinations and they validated their model with an experimental study. According to their results, melt-pool width and depth increases with laser power and decreases with scan speed [20]. A similar result was found in the experimental studies that were performed by Scime et al. in which the effect of process parameters on the formation of defects such as keyhole and balling were emphasized [23].

The process parameters significantly influence the formation of residual stresses and distortion of the deposited part [24, 25]. Accordingly, Mukherjee et al. concluded that thermal strains being directly proportional to the laser power and inversely proportional to the scan speed. Similarly, Simsons et al. studied the influence of energy density on the residual stresses which depended on the process parameters of laser power, scan speed, layer thickness, and hatch spacing [26]. They reported an increase in the residual stresses with increasing energy density. However, according to Bartlett et al., generic energy density expression was not a precise formulation for the actual energy density applied, and each parameter should be considered individually, because each parameter had a different effect on the residual stress [27]. Shiomi et al. reported a slight decrease in residual stresses with increasing scan speed [28]. The layer thickness is another important process parameter for the residual stresses of the deposited part. Mukherjee et al. concluded that using thin layers reduces the build-up of residual stresses while increasing distortions [24]. Anderson et al. reported that to reduce the residual stress and its gradients, the layer thickness shall be increased based on their experimental measurements, which were performed on LPBF manufactured specimens by using neutron diffraction [29]. The influence of process parameters on the residual stresses still not well understood that requires further research.

The scan strategy has an impact on the residual stresses after AM [30]. In practice, the scan direction rotates after completion of each layer with a default angular rotation of 90° or 67° about the build direction [31]. Parry et al. performed process simulations using a commercial software and its user subroutines to conclude that the scan pattern affects the residual stress distribution but not its magnitude [32]. Similarly, Bagg et al. conducted experiments to relate different scan strategies, such as continuous, island, and chess patterns, to compare the part distortion and residual stresses [33]. In that study, the largest distortions were found with the chess scan strategy, and the largest tensile stresses appeared with the continuous scan strategy. There is still a demand for a better understanding of the effect of the scan strategy on distortions and residual stresses.

Part-scale distortion and residual predictions require numerically efficient process models. For this reason, layer-by-layer simulation methods have been used for distortion predictions [34]. In addition, semi-quiet element method activation methods have been used [35]. Patil et al. developed an FE method that used two separate mesh refinement levels in one model [36]. Some models divide the part into sub-domains and apply a heat source simultaneously over the domain to simulate the process efficiently [37, 38]. Similar methods, such as simultaneous activation of multiple layers [18], adaptive meshing [39] and domain decomposition [40], have been developed to perform simulations in a computationally efficient manner.

The inherent strain method has been used to predict the residual deformations after the welding process efficiently [41, 42]. Similarly, eigenstrain construction methods have been developed to find stresses for processes involving thermal gradients [43, 44]. Ding et al. used the inherent strain method to determine the residual stresses after the wire and arc AM process approximately a hundred times faster than with thermomechanical process simulations [45]. The method was used with multi-scale models to compute the distortions and residual stresses at the part scale using inherent strains that were computed from meso and micro-scale simulations [46, 47]. The limitations of the inherent strain method have also been investigated [48], and different modified versions of this method have been presented [49].

In this study, a thermomechanical simulation model is developed at first, and it is implemented in a FE environment considering the temperature dependent properties of powder, solid, and liquid states. The inherent strain method (ISM) is also implemented to predict residual stresses from the thermal LPBF process simulations. The ISM and thermomechanical model results are compared to show the deliverables of the proposed LPBF process simulation model. In addition, a new method is used to represent surface heat losses as volumetric heat fluxes to eliminate the definition of surface fluxes after deposition of a layer. The thermomechanical model was used to predict the melt-pool dimensions, states, and residual stresses for different process parameters.

The paper is structured as follows. Sections 2 and 3 explain the thermomechanical and inherent strain modeling approaches in detail, respectively. Section 4 shows the experimental methods that were used provide comparison to the simulation findings. Sections 5 and 6 include the discussion of the results and conclusions, respectively.

2. Thermomechanical Model

2.1. Thermal Model

The thermal model includes a solution of the transient energy balance relation. In Eq. (1), ρ , C_p , T , \mathbf{q} , and \dot{Q} represent the mass density, specific heat, temperature, heat flux vector, and heat input, respectively. The heat flux vector and heat input are computed at position \mathbf{x} and at time t . \dot{q}_{conv} , \dot{q}_{rad} , and \dot{q}_{eva} represent the surface heat losses due to convection, radiation, and evaporation, respectively.

$$\rho C_p \frac{\partial T}{\partial t} = -\nabla \cdot \mathbf{q}(\mathbf{x}, t) + \dot{Q}(\mathbf{x}, t) - \dot{q}_{conv} - \dot{q}_{rad} - \dot{q}_{eva} \quad (1)$$

Goldak's double ellipsoid model is used as the heat input, as shown in Eq. (2). \dot{Q} is the heat input per unit volume, P is the laser beam power, and η is the lumped efficiency factor. r_x , r_y , and r_z represent the laser spot radii in the d_x , d_y , and d_z directions, respectively.

$$\dot{Q}(\mathbf{x}, t) = \frac{6\eta\sqrt{3}P}{\pi\sqrt{\pi}r_x r_y r_z} \exp\left(-\frac{3d_x^2}{r_x^2}\right) \exp\left(-\frac{3d_y^2}{r_y^2}\right) \exp\left(-\frac{3d_z^2}{r_z^2}\right) \quad (2)$$

The heat flux vector, \mathbf{q} , is computed using the temperature gradients as given in Eq. (3).

$$\mathbf{q}(\mathbf{x}, t) = -\mathbf{k} \nabla T \quad (3)$$

Conductivity is assumed for homogeneous media with only the diagonal terms along the longitudinal, lateral, and depth directions that are represented by k_x , k_y , and k_z in Eq. (4).

$$\mathbf{k} = \begin{bmatrix} k_x & 0 & 0 \\ 0 & k_y & 0 \\ 0 & 0 & k_z \end{bmatrix} \quad (4)$$

Convection is considered in the model. The corresponding heat loss from the surfaces, $\dot{q}_{conv}(\mathbf{x}_s, t)$, is computed using an effective convection coefficient, h , and ambient temperature, T_0 , as given in Eq. (5). \mathbf{x}_s denotes the surface-position vector.

$$\dot{q}_{conv}(\mathbf{x}_s, t) = h(T - T_0) \quad (5)$$

The radiative heat loss from the exposed surfaces, $\dot{q}_{rad}(\mathbf{x}_s, t)$, is computed using Eq. (6), where ϵ and K_B are the emissivity and Boltzmann constant, respectively.

$$\dot{q}_{rad}(\mathbf{x}_s, t) = \epsilon K_B (T^4 - T_0^4) \quad (6)$$

The evaporative heat loss, $\dot{q}_{eva}(\mathbf{x}_s, t)$, is calculated using Eq. (7) in accordance with [50]. ΔH_ν^* , M , R , T_s , T_ν , and P_0 are the effective enthalpy of the metal vapor, molar mass of the metal vapor, universal gas constant, temperature of the surface, boiling temperature, and

atmospheric pressure, respectively.

$$\dot{q}_{eva}(\mathbf{x}_s, t) = \frac{0.82 \Delta H_\nu^*}{\sqrt{2} \pi M R T_s} P_0 \exp\left(\frac{\Delta H_\nu^* (T_s - T_\nu)}{R T_s T_\nu}\right) \quad (7)$$

2.2. Mechanical Model

The local form of equilibrium is expressed with Eq. (8) for a static case without any body force.

$$\nabla \cdot \boldsymbol{\sigma} = \mathbf{0} \quad (8)$$

The total strain, $\boldsymbol{\epsilon}$, can be decomposed into its elastic, $\boldsymbol{\epsilon}_e$, plastic, $\boldsymbol{\epsilon}_p$, and thermal $\boldsymbol{\epsilon}_T$ strain components, as expressed by Eq. (9).

$$\boldsymbol{\epsilon} = \boldsymbol{\epsilon}_e + \boldsymbol{\epsilon}_p + \boldsymbol{\epsilon}_T \quad (9)$$

The numerical solution is based on incremental form of strain, hence incremental form of Eq. (9) becomes as in Eq. (10) in which $\Delta \boldsymbol{\epsilon}$ represents the given increment of total strain.

$$\Delta \boldsymbol{\epsilon} = \Delta \boldsymbol{\epsilon}_e + \Delta \boldsymbol{\epsilon}_p + \Delta \boldsymbol{\epsilon}_T \quad (10)$$

Thermal strain increment is computed by multiplying the thermal expansion coefficient, $\alpha(T)$, which is a function of temperature, with the temperature increment, ΔT , as in Eq. (11).

$$\Delta \boldsymbol{\epsilon}_T = \alpha(T) \Delta T \quad (11)$$

Trial stress, $\boldsymbol{\sigma}^{tr}$, is calculated assuming all of the strain increment is elastic using elasticity, as in Eq. (12).

$$\boldsymbol{\sigma}^{tr} = \mathbf{C} : \Delta \boldsymbol{\epsilon} \quad (12)$$

Deviatoric part of trial stress, $\boldsymbol{\sigma}^{tr'}$, is calculated using Eq. (13).

$$\boldsymbol{\sigma}^{tr'} = \boldsymbol{\sigma}^{tr} - \frac{\mathbf{I}}{3}(\boldsymbol{\sigma}^{tr} : \mathbf{I}) \quad (13)$$

Von Mises trial stress, σ_{VM}^{tr} , is the scalar measure for the driving stress for plasticity that is computed from the deviatoric part of the trial stress, $\boldsymbol{\sigma}_{dev}^{tr}$, as in Eq. (14).

$$\sigma_{VM}^{tr} = \sqrt{\frac{3}{2} \boldsymbol{\sigma}^{tr'} : \boldsymbol{\sigma}^{tr'}} \quad (14)$$

The plastic flow direction, \mathbf{n}_p , is computed from the trial deviatoric stress using Eq. (15) based on normality principle.

$$\mathbf{n}_p = \frac{3}{2} \frac{\boldsymbol{\sigma}^{tr'}}{\sigma_{VM}^{tr}} \quad (15)$$

The plastic strain increment is computed using the flow direction, \mathbf{n}_p , based on normality

rule with plastic strain increment, Δp , as shown in Eq. (16).

$$\Delta \epsilon_p = \mathbf{n}_p \Delta p \quad (16)$$

The plastic strain increment is coupled with the stresses through a flow rule or yield function, ψ , that is a function of temperature. Consistency requires Eq. (17) to hold during plasticity.

$$\psi(\boldsymbol{\sigma}, \Delta p) = \sigma_{VM} - \sigma_y(\Delta p, T) = 0 \quad (17)$$

Once the thermal and plastic strain increments are calculated, the elastic strain increment and the corresponding stress are computed using Eqs. (10) and (12), respectively. The solution for the plastic strain increment (or stress) is obtained by iteratively until the increment is less than a convergence tolerance. In this study, an isotropic elastic-perfectly plastic model is employed. The same model is applied to the baseplate and build material considering different material properties. In case the material state of active element is either powder or liquid, a low value of elastic modulus (0.1 GPa) is used to compute the material tangent and the stresses are assumed to vanish.

2.3. Finite Element Model

The local problem is converted into an FE problem by discretization of temperatures, as in Eq. (18) [51].

$$T(\mathbf{x}) = \mathbf{N}(\mathbf{x}) \hat{\mathbf{T}} \quad (18)$$

The weak form of the energy balance is obtained by discretizing the temperatures and multiplying the energy balance with a weight function followed by integration. The solution of Eq. (19) gives nodal temperatures $\hat{\mathbf{T}}$, for boundary conditions [52].

$$\left[\int_V \mathbf{N}^T \rho C_p \mathbf{N} dV \right] \frac{\hat{\mathbf{T}} - \hat{\mathbf{T}}_t}{\Delta t} + \left[\int_V \nabla \mathbf{N}^T \mathbf{k} \nabla \mathbf{N} dV \right] \hat{\mathbf{T}} = \int_V \mathbf{N}^T \dot{Q} dV - \int_S \mathbf{N}_s^T \mathbf{q}_s \cdot \mathbf{n} dS \quad (19)$$

q_{eff} represents effective surface heat losses due to convection, radiation, and evaporation through the top surface of the topmost elements (Eq. (20)).

$$\dot{q}_{eff} = \dot{q}_{conv} + \dot{q}_{rad} + \dot{q}_{eva} \quad (20)$$

In the FE model, after the addition of a new layer of material, the traction-free surfaces must be defined to identify heat losses.

Figure 1(a) shows the surface losses of \mathbf{q}^* and \mathbf{q}^{**} from two surfaces dS^* and dS^{**} with the corresponding surface normals of \mathbf{n}^* and \mathbf{n}^{**} , respectively. The total loss can be expressed as in Eq. (21) [53].

$$\int_S (\mathbf{q}^* \cdot \mathbf{n}^* + \mathbf{q}^{**} \cdot \mathbf{n}^{**}) dS = \int_V \nabla \cdot \mathbf{q} dV \quad (21)$$

Figure 1(b) shows the surface losses on a single finite element during the AM process in

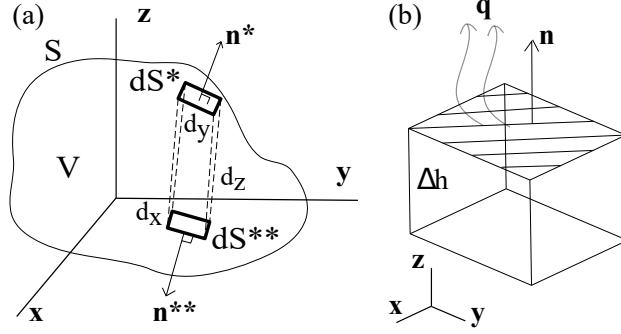


Figure 1: Conversion of surface fluxes to volumetric heat loss term (a) general surface losses from a body, (b) a finite element with surface flux from its top surface.

which the effective heat loss is in the form of a surface flux which is applied only on the top surface. Therefore, the surface integral is converted into volume integrals by dividing the flux by the thickness of the element, as in Eq. (22). In this study, one element per thickness direction is used for each layer; hence, the surface heat flux, \mathbf{q}_s , is obtained by division of the effective surface flux to the layer thickness, Δh . This term is applied to the model together with the volumetric heat input.

$$\int_S \mathbf{q}_s \cdot \mathbf{n} dS = \int_V \nabla \cdot \mathbf{q}_s dV = \int_V \frac{q_{eff}}{\Delta h} dV \quad (22)$$

The energy balance is solved at each time step until the temperature update for an iteration cycle becomes smaller than a tolerance; in this study, 100 K was used as the tolerance value.

The mechanical equilibrium invokes a solution for the displacements; hence, the displacements are discretized, as in Eq. (23).

$$\mathbf{u}(\mathbf{x}) = \mathbf{N}(\mathbf{x}) \hat{\mathbf{u}} \quad (23)$$

Strains are obtained through strain-displacement coupling, \mathbf{B} , as in Eq. (24).

$$\boldsymbol{\epsilon} = \mathbf{B} \hat{\mathbf{u}} \quad (24)$$

The weak form of equilibrium is obtained by multiplying the local form in Eq. (8) with the weight function and integrating the result over the volume of the domain. Eq. (25) shows the discrete form of mechanical equilibrium.

$$\int_V \mathbf{B}^T \boldsymbol{\sigma} dV = \mathbf{0} \quad (25)$$

MATLAB[®] is used to generate the inputs for the FE model, mesh file, input file for analysis (i.e., process parameters, material constants), and parameters for path generation at the initialization stage for efficient and consistent generation of the model. MSC MARC[®]

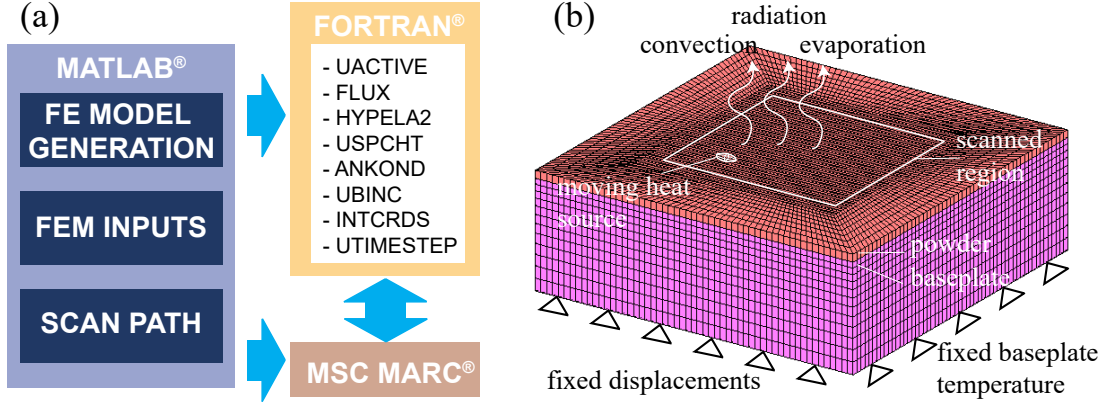


Figure 2: (a) Finite element model generation including the inputs, constants, and a list of the user-subroutines that are utilized in the thermomechanical finite element analysis. (b) Mesh and boundary conditions of finite element model.

is used as the FE environment with its available user subroutines that are in Fortran[®] language, as shown in Figure 2(a).

Figure 2(b) shows the FE model and boundary conditions. Fixed displacements and a fixed temperature of 323 K (50°C) are applied to the bottom surface of the baseplate as the boundary conditions.

Several subroutines are used together in the simulations. Finite element solver visits the subroutines UACTIVE, USPCHT, ANKOND, FLUX, and HYPELA2 for every element, integration point, during every increment, and iteration cycle. Detailed description of the user-defined subroutines is as follows:

- UBINC sets up the initial values of global variables and updates the state variables used in the thermal and mechanical field solvers at the beginning of each increment. The first call and corresponding initialization of the software is performed within this subroutine.
- UTIMESTEP is used to set the minimum and maximum limits for the time increment based on the position of the heat source which is determined by the absolute time. The time stepping is determined based on the convergence criteria. During the recoating or cooling stages larger initial time steps are enforced.
- UACTIVE activates the elements at the powder state after recoating cycle before the deposition of a layer. The build elements are deactivated initially only and baseplate elements are active all the time during the process simulations. The activation criteria is based on the absolute time of the simulation depending on the position of the heat source along build direction.
- INTCRDS gives the integration point coordinates of each element which is used only once at the beginning of the calculations.
- USPCHT is used to enter the specific heat that depends on the material type (baseplate or build layer), state (powder/liquid/solid), and temperature.

- ANKOND is used to enter the anisotropic conductivity constants along x, y, and z directions that depends on the material type (baseplate or build layer), state (powder/liquid/solid), and temperature. This subroutine is used to incorporate Maragoni effect by increasing conductivity along longitudinal direction with a factor at liquid state, k_x .
- FLUX is used to enter the coordinates and magnitude of the volumetric moving heat flux. Surface heat losses are also entered as negative heat sources for the topmost elements in the layer only. This subroutine is defined for only the build elements for time efficiency. Thermal solver visits this subroutine only for the active elements in the mesh.
- HYPELA2 is used for the mechanical user-defined solver for different states of the material. This subroutine has access to the temperatures and hence it is used to enter temperature dependent mechanical constitutive models for powder/liquid/solid phases. Different mechanical properties for the baseplate and build elements are used. Similarly, zero stress values with low stiffness properties are used to define mechanical response of powder and liquid states. Mechanical solver enters HYPELA2 only for the active elements.

2.4. Mesh sensitivity

A mesh sensitivity study is conducted to select a proper mesh size for the FE model in the scanned region. The mesh convergence study is performed for single layer deposition using the process parameters shown in Table 1. The reference mesh size value of 50 μm is used which is equal to the radius of the laser beam. Figure 3(a) shows the maximum and minimum temperatures with respect to the mesh refinement level. A higher percentage indicates a finer mesh. Mesh refinement level significantly effects the magnitude of the minimum and maximum temperatures. The minimum temperature takes values below the baseplate temperature (323 K) for mesh refinement levels less than 60%. Similarly, minimum temperatures reach almost absolute zero for mesh refinements coarser than 30%, the revealed highly inaccurate results. This observation is attributed to the intense heat source input, causing a very sharp temperature gradient near the melt-pool. Both the minimum and maximum temperatures have convergent behavior for mesh refinement levels that are finer than 60%.

The mesh refinement does not impact the equivalent Von Mises stresses significantly because the stresses are approximately equal to the yield strength as shown in Figure 3(b). In contrast, the longitudinal stress component reached a steady value at 50% mesh refinement, as shown in Figure 3(b). Considering the computational time, a mesh refinement of 60% is selected as the minimum refinement necessary to obtain temperatures and the stresses accurately. The converged solution consists of a mesh with 113409 number of nodes and 99200 elements in total.

2.5. Material Properties

Two types of material models are used in the model: baseplate and build material. Table A.1 show the constant properties of baseplate (SS316). Figures A.1 and A.2 show

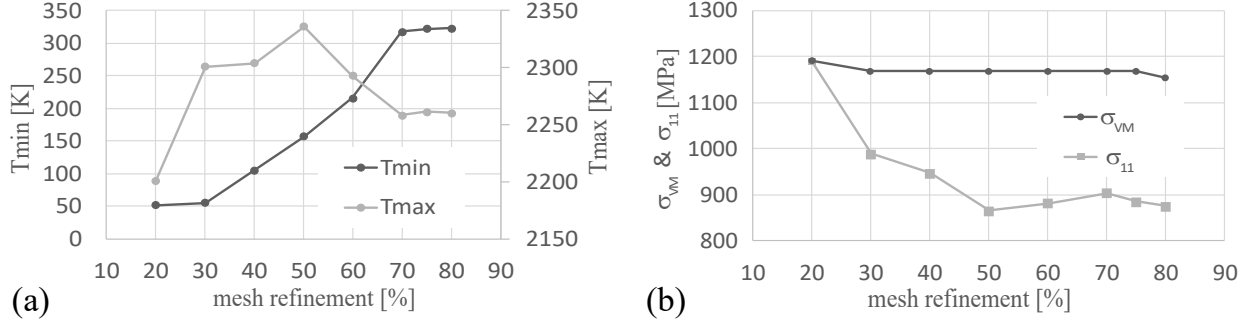


Figure 3: Mesh sensitivity study for **a.** temperature, **b.** longitudinal stress and Von Mises stress. Percentage mesh refinements were computed using a reference mesh size of 50 μm

the temperature-dependent build material (IN718) properties. The following definitions for material properties are implemented in the user-defined subroutines of the finite element solver.

The build material consists of three different states: powder, liquid, and solid. ω is used as an indicator to account for these different material states¹.

- powder ($\omega = -1$)
- liquid ($\omega = 0$)
- solid ($\omega = 1$)

Any property in the liquid-solid state transformation regime, that is also referred as the mushy regime, is computed by the rule of mixtures. Eq. (26) shows the application of the rule of mixtures method to find the property at the corresponding state by using the solid, ρ_s , and liquid, ρ_l , phases to determine the mass density in the mushy regime, ρ [54].

$$\rho = \omega \rho^{(s)} + (1 - \omega) \rho^{(l)} \quad (26)$$

The powder material properties are computed using the properties of solid and the porosity of the powder bed, φ . Direct proportionality is used to calculate the density, $\rho^{(p)}$, and specific heat, $C_p^{(p)}$, of the powder from the corresponding solid properties, $\rho^{(s)}$ and $C_p^{(s)}$, as in Equations (27) and (28). A powder porosity, φ , of 0.4 was used in the calculations [16].

$$\rho^{(p)} = (1 - \varphi) \rho^{(s)} \quad (27)$$

$$C_p^{(p)} = (1 - \varphi) C_p^{(s)} \quad (28)$$

Specific heat or heat capacitance shall be modified to take into account the latent heat

¹The state of the properties are represented by the superscripts '(p)', '(s)', and '(l)' for the powder, solid, and liquid states, respectively. That is, $C_p^{(s)}$ is the specific heat of the solid

effects [55]. In this study, the latent heat effects were not considered. The latent effect would help reduce the number of iteration cycles of thermal solution by reducing the maximum temperatures thereby decreasing the number of cycles required for a temperature increment.

The thermal conductivity of the powder material properties is computed using the solid material properties and the powder porosity in the powder bed, φ , in accordance with the reference [56]. In Eq. (29), $k^{(Ar)}$'s the conductivity of argon gas surrounding the powder particles and $k^{(s)}$ is the conductivity of the solid metal.

$$k^{(\varphi)} = k^{(Ar)} \left[(1-a) \frac{\varphi f_0 + \frac{k^{(s)}}{k^{(Ar)}}(1 - \varphi f_0)}{1 - \varphi(1 - f_0) + \frac{k^{(s)}}{k^{(Ar)}}\varphi(1 - f_0)} + a \frac{2 \left(\frac{k^{(s)}}{k^{(Ar)}} \right)^2 (1 - \varphi) + (1 + 2\varphi) \frac{k^{(s)}}{k^{(Ar)}}}{(2 + \varphi) \frac{k^{(s)}}{k^{(Ar)}} + 1 - \varphi} \right] \quad (29)$$

f_0 is a function between 0-1 for scaling conductivity, which is given by Eq. (30).

$$f_0 = 0.8 + 0.1\varphi \quad (30)$$

The scaling factor, a , is a function of the powder bed porosity (Eq. (2.5)).

$$\log(a) = \begin{cases} -4.898\varphi, & 0 \leq \varphi < 0.0827 \\ -0.405 - 3.154(\varphi - 0.0827), & 0.0827 \leq \varphi < 0.298 \\ -1.084 - 6.778(\varphi - 0.298), & 0.298 \leq \varphi < 0.580 \end{cases}$$

The conductivity of the liquid state along the scan direction (k_x) is assumed to be 1.5 times higher than its actual magnitude to account for the enhanced heat transfer inside the melt-pool due to the Marangoni effect. Table A.1 shows the values of temperature-dependent conductivity for IN718.

The emissivity of the powder particles, $\varepsilon^{(p)}$, is computed from the emissivity of the same material in the solid phase, $\varepsilon^{(s)}$, considering the radiation between the powder particles, Eq. (31).

$$\varepsilon^{(p)} = A^{(H)} \varepsilon^{(H)} + (1 - A^{(H)}) \varepsilon^{(s)} \quad (31)$$

The area fraction of the surface, $A^{(H)}$, refers to the areal fraction of the voids in a porous medium (Eq. (32)).

$$A^{(H)} = \frac{0.908\varphi}{1.908\varphi - \varphi^2 + 1} \quad (32)$$

The emissivity, $\varepsilon^{(H)}$, in porous media is calculated using Eq. (33).

$$\varepsilon^{(H)} = \frac{\varepsilon^{(s)} \left[2 + 3.082 \left(\frac{1 - \varphi}{\varphi} \right)^2 \right]}{\varepsilon^{(s)} \left[1 + 3.082 \left(\frac{1 - \varphi}{\varphi} \right)^2 \right] + 1} \quad (33)$$

2.6. Time stepping procedure

Two different time intervals are used in the model: single scan vector time (scan time), and re-coating time. The single scan vector time is divided by time increments of Δt_{scan} . After the completion of a layer, the recoating time, Δt_{recoat} , is applied to account for the cooling during spreading of new powder with a recoating blade, as in the actual process. Although the recoating is usually complete within seconds in a real LPBF process, the re-coating time in the simulations is selected to be much less, that is sufficient enough for the model to cool down to the baseplate temperature completely considering due to the high cooling rates (10^4 K/s).

The time step during the deposition, Δt_{scan} , is determined automatically by setting the tolerance value for temperature increment to 50 K. The solution algorithm reduces the time step, if necessary, starting from a predefined magnitude down to a prescribed minimum value. The maximum time step was selected such that the position change of the heat source during the time step lies within the effective radius of the laser beam, r , in accordance with Eq. (34), which is similar to that in [32].

$$\Delta t_{scan} < \frac{r}{v} \quad (34)$$

The effective size of the region, r , is calculated from the beam size using Eq. (35).

$$r = \sqrt{r_x^2 + r_y^2 + r_z^2} \quad (35)$$

The time step must be selected considering the thermal shock effects; otherwise, negative temperatures can be observed in the simulations. To avoid this, the restriction in Eq. (36) is used in the time step during scanning, Δt_{scan} , in which L is the characteristic element size along the scan direction, k_x is the conductivity along the scan direction, ρ is the density, and C_p is the specific heat of the material [57].

$$\Delta t_{scan} > \frac{L^2 \rho C_p}{k_x} \quad (36)$$

2.7. Process Parameters

Table 1 lists the process parameters for selective laser melting, which include laser power, scan speed, beam radii, hatch spacing, and layer thickness.

Table 1: Default process parameters for selective laser melting of EOS-M209 LPBF system [31].

laser power	scan speed	beam radii	hatch spacing	layer thickness	efficiency
P	v	r_x, r_y, r_z	Δd	Δh	η
[W]	[mm/s]	[μm]	[μm]	[μm]	-
285	960	50 / 50 / 125	110	40	0.3

The efficiency factor, η , is different for the powder and solid states. A larger efficiency is used for the powder state, $\eta^{(p)} = 0.6$, than for the solid state, $\eta^{(s)} = 0.3$.

3. Inherent Strain Method

The inherent strain method (ISM) is used to calculate stresses instead of strains from temperature distributions in the current study. Inherent strains, ϵ_{IS} , are computed based on the maximum temperatures [41]. ISM computes the strains based on the certain temperature limiting values. Eq. (37) shows the criteria based on the temperature limits T_1 and T_2 . β represents the magnitude of rigidity constraints along each direction, and it takes a value between 0 and 1.

$$\epsilon_{IS} = \begin{cases} 0, & T_{max} < T_1 \\ -\alpha T_{max} + \sigma_y/E/\beta & T_1 < T_{max} < T_2 \\ -\sigma_y/E/\beta & T_2 < T_{max} \end{cases} \quad (37)$$

The temperature limits are related to the material properties and rigidity constraints with Eqs. (38) and (39).

$$T_1 = \sigma_y/E/\alpha/\beta + T_0 \quad (38)$$

$$T_2 = 2T_1 \quad (39)$$

In the original inherent strain formulation [41], the longitudinal direction (x-direction) was aligned with the weld or velocity vector. Therefore, in the previous studies, welding directions were always along the longitudinal direction, which did not require any transformation [45, 58] which is the same in the current study. However, to keep generality for AM processes rotation, \mathbf{R} , has to be defined to transform the stresses, \mathbf{S} , at the reference frame defined with scan direction to the sample reference, Eq. (40).

$$\boldsymbol{\sigma} = \mathbf{R} \mathbf{S} \mathbf{R}^T \quad (40)$$

Transformation involves rotations, \mathbf{R} , in which θ is the rotation angle about the build direction (z-axis of the sample reference), as in Eq. (41). The direction of the scan in the plane, θ , needs to be known or entered for each layer in this case. In the current study the scan direction is the same as x-direction of the sample giving $\theta = 0^\circ$.

$$\mathbf{R} = \begin{bmatrix} \cos(\theta) & \sin(\theta) & 0 \\ -\sin(\theta) & \cos(\theta) & 0 \\ 0 & 0 & 1 \end{bmatrix} \quad (41)$$

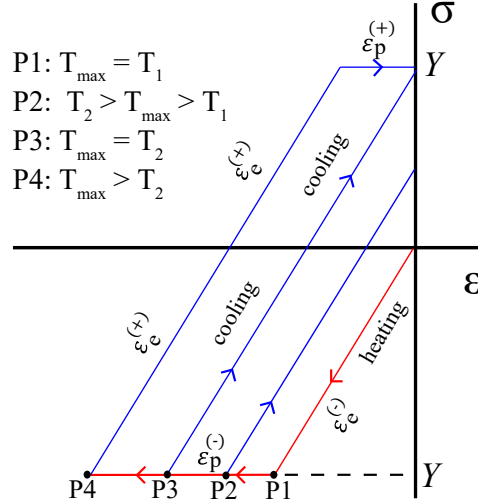


Figure 4: Schematic sketch of stress-strain diagram during cooling of a single material point.

In the case of inherent strain method, only the thermal problem was solved, and the maximum temperature values are stored for each integration point of each finite element. The stresses are then computed by subsequent addition of a layer with inherent strains and quasi-static mechanical solutions for the displacement field [41, 42, 45, 58].

Figure 4 illustrates the thermal cycle of a material during deposition schematically. Eq. 42 and Eq. 43 relate temperatures to inherent strains. As the material heats up, the displacement constraint prevents thermal expansion of the build layer that leads to compressive strains. If the stresses exceed the yield stress, plastic straining starts which results in the formation of residual compressive strains and tensile stresses after the cooling down. Therefore, the amount of plastic straining occurs in both heating and cooling stages depending on a critical temperature, $T_{max}=T_2$. Temperature limits T_1 and T_2 are also dependent on rigidity constraints that are similar to spring stiffness. Because the constraint in the longitudinal direction is greater than that of the transverse direction, T_{1y} is larger than T_{2x} . Hence, even though the maximum temperature within the material exceeds T_{1x} , only the compressive plastic strain occurs in the longitudinal direction up to $T_{max}=T_{2x}$, and it is a function of T_{max} . In case T_{max} exceeds T_{2x} , further plastic strain at both the heating (compressive) and cooling (tensile) stages, the residual stresses will retain their magnitude, the same as the yield stress along the longitudinal direction. In this regime, the plastic strain becomes proportional to T_{max} , as shown in Eq. 43 along the transverse direction. C is a constant that is computed as $C = T_{2x}$ from the continuity condition of Equations 43 and 45. A is an unknown constant that needs to be determined by calibration. This mechanism was also discussed in previous studies [28].

$$\epsilon_{xx} = \begin{cases} 0, & T_{max} < T_{1x} \\ -\alpha T_{max} + \sigma_y/E/\beta_x & T_{1x} < T_{max} < T_{2x} \\ -\sigma_y/E/\beta_x & T_{2x} < T_{max} \end{cases} \quad (42)$$

$$\epsilon_{yy} = \begin{cases} 0, & T_{max} < T_{2x} \\ -A\alpha(T_{max} - C) & T_{2x} < T_{max} \end{cases} \quad (43)$$

ISM predicts stresses by using only the thermal solution, more precisely the maximum temperatures, T_{max} . The maximum stress in the longitudinal direction is assumed to be equal to the yield stress if T_{max} exceeds T_{2x} . On the other hand, the transverse component of stress is assumed to be a function of T_{max} , as shown in Figure 4.

The constant A_s needs to be calibrated using the results of thermomechanical simulations as a function of the maximum temperatures, T_{max} . Note that calibration can also be done experimentally. The calibration was performed using only for a set of process parameters. The magnitudes of T_{max} and σ_{yy} were collected from thermomechanical simulations for three different laser power levels which allowed to investigate the effect of different T_{max} values.

$$\sigma_{xx} = \begin{cases} 0, & T_{max} < T_{2x} \\ \sigma_y, & T_{2x} < T_{max} \end{cases} \quad (44)$$

$$\sigma_{yy} = \begin{cases} 0, & T_{max} < T_{2x} \\ A_s E \alpha (T_{max} - C), & T_{2x} < T_{max} \end{cases} \quad (45)$$

In this study, the stress components along longitudinal and transverse directions were obtained using Equations (44) and (45). Finally, the magnitudes and distributions of these stresses were predicted using only the T_{max} value at each integration point of every element, which were determined from the thermal simulations for any given process parameters.

4. Experimental

Experimental studies include analysis of cross-sections of deposited specimens that were manufactured with different levels of laser power. The manufacturing of the samples were performed using EOS-M290 LPBF system. Single tracks of IN718 material were deposited on SS316 base plate. Three different laser power values were used as 160 W, 190 W, and 220 W with the default scan speed of 960 mm/s. 40 mm length was used in the tracks and each track was transversely positioned 3 mm away from each other to prevent any interaction between the build single tracks. Cross-section of build layers of single track samples were investigated to find the dimensions of the melt-pool size to validate the proposed thermal model.

The samples were cut in the middle using abrasive water-jet cutting process. Next, epoxy resin and hardener used to apply cold mounting. Then, wet polishing was applied using SiC grinding papers to the cross-sectioned surfaces. After that, surfaces were etched with a

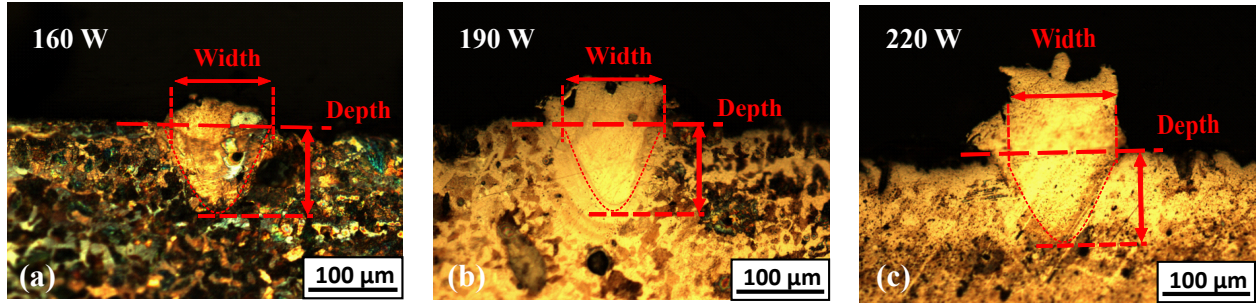


Figure 5: Melt-pool images obtained for laser power magnitudes of (a) 160 W, (b) 190 W, and (c) 220 W at a scan speed of 960 mm/s.

equal mixture of HCl, CH₃COOH and HNO₃. Finally, melt-pool images were obtained by Nikon LV1000ND optical microscope as shown in Figure 5. Dimensions of melt-pools were measured using a raster graphics editor. Each optical measurement was performed ten times to quantify measurement uncertainties. Depth of the melt-pools were measured with respect to the baseplate level using a similar method as in the reference [59].

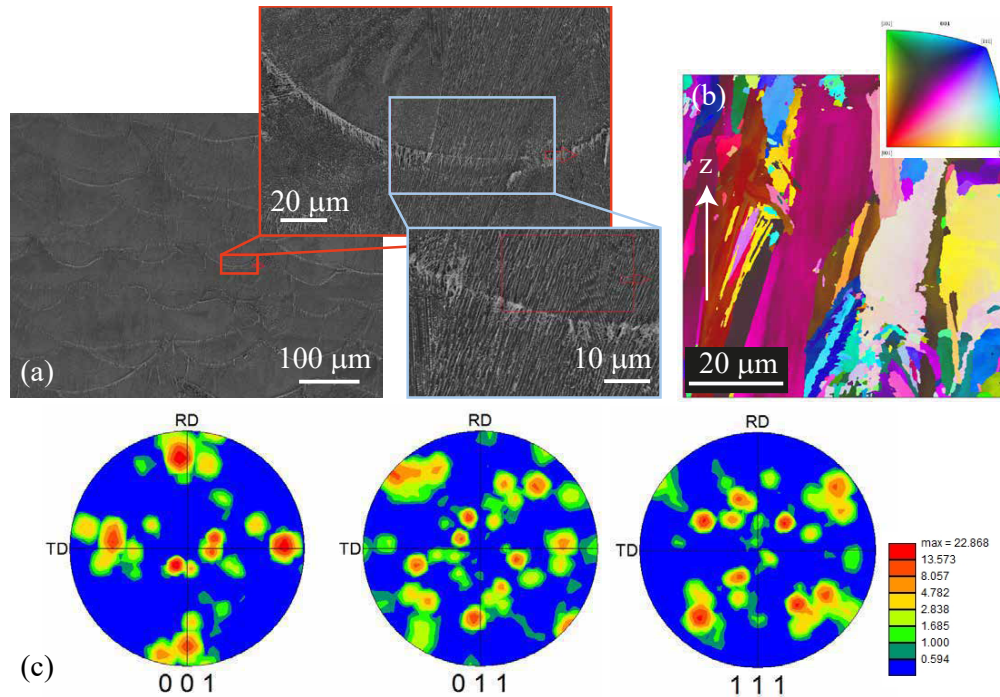


Figure 6: Experimental characterization of a test sample with multi layer builds that was manufactured with the default process parameters of 285 W, 960 mm/s, 80 μ m of laser power, scan speed, and layer thickness, respectively. (a) SEM images with different magnification, (b) EBSD map, (c) texture pole figures (RD is along the build direction.).

Another large cube sample was prepared with 10 mm edge length using the standard manufacturing parameters of EOS-M290 LPBF system. The process parameters were 285 W, 960 mm/s, 80 μ m for laser power, scan speed, and layer thickness, respectively. Sample was wet ground and polished with a final solution of colloidal silica. The analysis was performed

using ZEISS-Cross beam scanning electron microscopy (SEM) and electron backscattered diffraction (EBSD) system. Figure 6 shows results of the micro scale characterization of a test sample. SEM images shows a uniform fusion of the melt zones with each other. The melt zone structures consisted of needle-like dendritic structures, Figure 6(a). High resolution EBSD analysis of the cross-section shows large grains with growth along the build direction, Figure 6(b). In addition, the texture pole figures reveals the presence of a cube texture in the material, Figure 6(c). Therefore, the build material had proper fusion of deposited layers having both crystallographic and morphological texture. Although a less sharper texture is expected in case lower laser power levels were used for IN718 [60]. The presence of significant amount of texture challenges the isotropic assumption used in the model and suggest the use of a texture-based calculation of thermal and mechanical properties of the material such as thermal conductivity, elastic modulus, and yield stress.

5. Results and Discussion

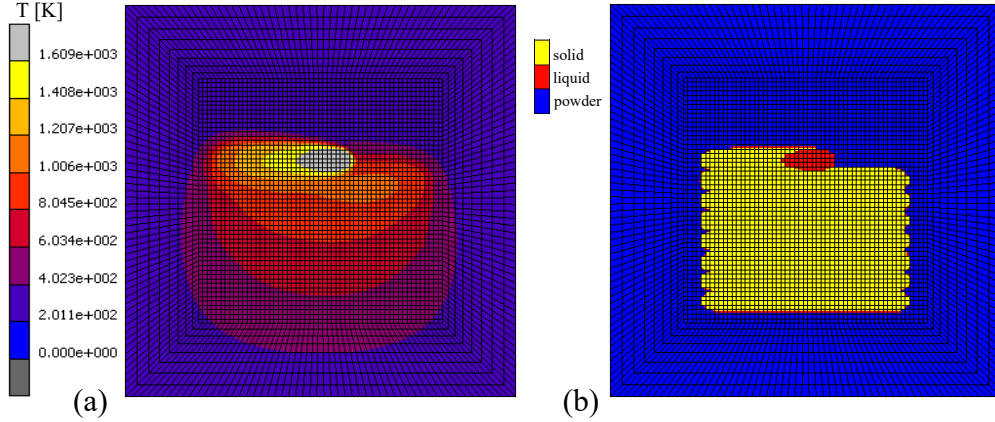


Figure 7: (a) Temperature distribution and (b) state of the material phase during deposition of first layer at $t=0.00899$ s. Process parameters: $P = 160$ W, $v = 1000$ mm/s, $\Delta d = 90$ μ m, $\Delta h = 40$ μ m, and unidirectional scan pattern.

Figure 7 shows the instantaneous distributions of temperatures and material states during the deposition of the first layer of the thermomechanical model. The laser power, scan speed, hatch spacing, and layer thickness were 160 W, 1000 mm/s, 90 μ m, 40 μ m, respectively and a uni-directional scan pattern was used in the simulations. The melt region is indicated with a gray colored contour in Figure 7(a). The conductivity of the material in the powder phase is much lower than that of the solid or liquid phases that leads to the asymmetric temperature distribution. Therefore, higher temperatures were computed on the solidified region in comparison to powder region with much lower thermal conductivity. Figure 7(b) shows the instantaneous states of powder, solid and liquid during deposition.

Table 2 shows the values of the process parameters that were used in the simulations; laser power, scan speed, hatch spacing, layer thickness, and scan pattern.

Table 3 shows the melt-pool dimensions with respect to different process parameters that were obtained from the thermomechanical simulations. The simulation results were collected

Table 2: Process parameters that were used in the simulations.

laser power	scan speed	hatch spacing	layer thickness	scan pattern
P	v	Δd	Δh	-
[W]	[mm/s]	[μm]	[μm]	-
160	600	75	30	unidirectional
190	1000	90	40	zigzag
220	1200	100	50	-

at the instant when the laser was in the middle of the fifth scan vector, after the deposition of one half of the hatch, or at the center of the printed layer. As the laser power increases, the melt-pool expands in all directions at approximately at the same rate. Increasing the scan speed decreases the amount of heat energy input per unit volume of material and consequently, both the depth and width of the melt-pool become smaller. Similarly, the melt-pool slightly shortens along the scan direction; however, at the same time, increasing speed tends to stretch the melt zone longitudinally. As a result, the length of the melt-pool barely decreases and does not become influenced by the scan speed as much as the other directions. Variations in layer thickness and hatch spacing do not have a significant effect on the melt-pool size.

Table 3: Melt-pool dimensions for altering process parameters

laser power	scan speed	hatch spacing	layer thickness	width	depth	length
[W]	[mm/s]	[μm]	[μm]	[μm]	[μm]	[μm]
160	1000	90	40	124	77	276
190	1000	90	40	130	86	333
220	1000	90	40	149	93	402
160	600	90	40	160	95	284
160	1200	90	40	121	68	272
160	1000	75	40	122	81	274
160	1000	100	40	127	78	281
160	1000	90	30	121	72	265
160	1000	90	50	123	76	283

Figure 8 shows the temperature distribution within the melt-pool for the following process parameters: laser power of 160 W, scan speed of 1000 mm/s, hatch spacing of 90 μm , and layer thickness of 40 μm . The melt-pool dimensions were calculated based on the width and depth dimension indicated in Figure 8(a) and (b), respectively.

Melt-pool dimensions from the cross-sections were also obtained from single track simulations and compared to the experimental findings to identify the simulation accuracy. Figure 9 shows the image of the melt-pool obtained from the experimental study and from the simulations for the same process parameters ($P = 190$ W, $v = 960$ mm/s, and $\Delta h = 40$ μm .). The track lengths were 1 mm long, the same as in the simulations which was selected for simulation efficiency.

In Table 4 melt dimensions that were measured from experimental cross-sections are compared with the values obtained from the simulations. The difference in the experiments and simulations (error) was less than 10% in both width and depth directions for three different laser power values. This clearly shows accurate predictive capacity of the melt-pool dimensions with the proposed model.

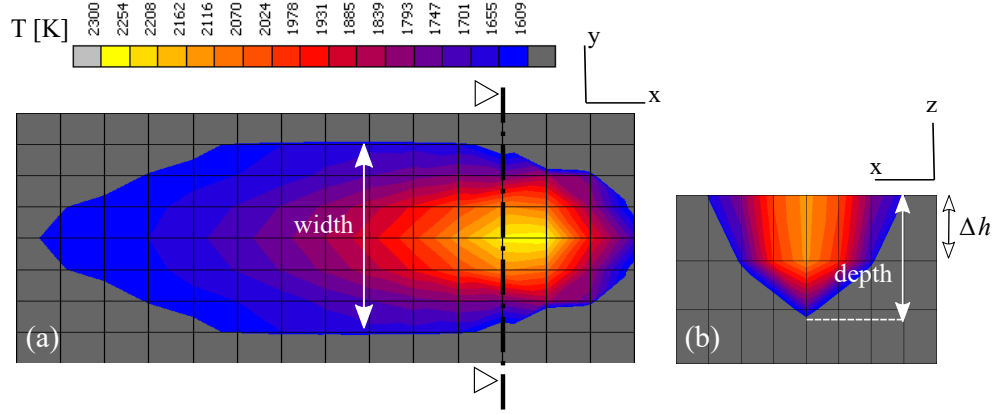


Figure 8: Melt-pool during deposition (a)top view and (b) cross-sectional view. $P = 160$ W, $v = 1000$ mm/s, $\Delta d = 90$ μm , $\Delta h = 40$ μm , and uni-directional scan pattern.

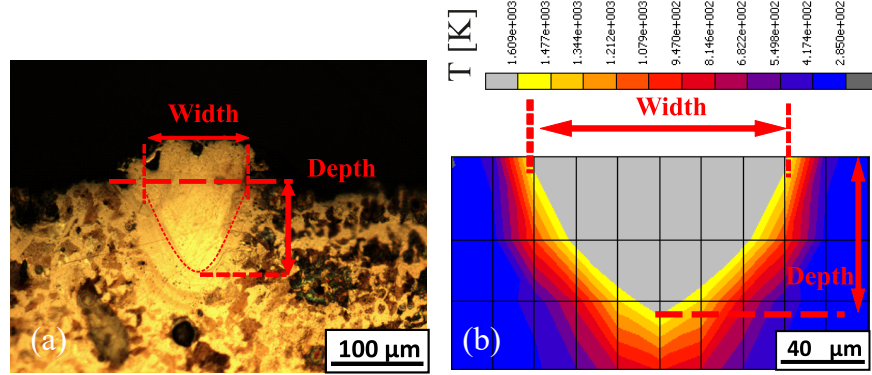


Figure 9: Melt-pool cross sections from (a) experimental study and (b) simulation from a single track deposition. $P = 190$ W, $v = 960$ mm/s, and $\Delta h = 40$ μm .

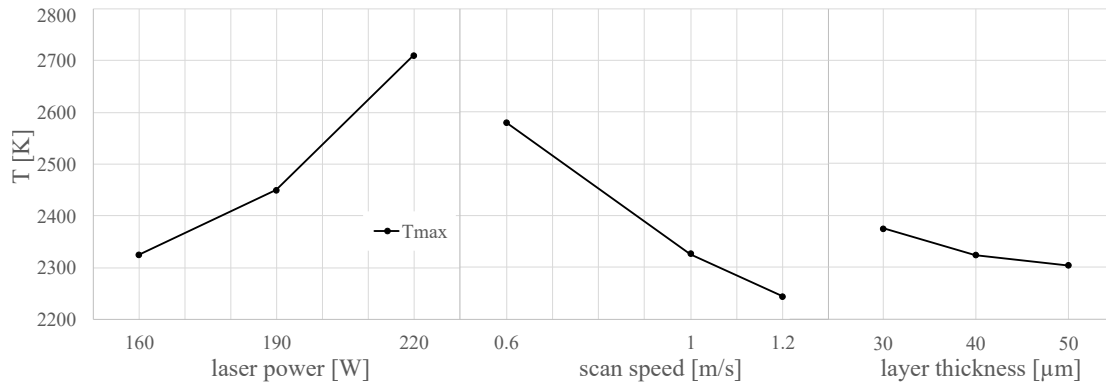


Figure 10: Effect of laser power, scan speed and layer thickness on the maximum temperature.

Figure 10 shows the variation of the maximum temperature with respect to process parameters. As expected, the maximum temperature was directly proportional to the laser power and inversely proportional to the scan speed similar to literature findings [61]. Increase-

Table 4: Comparison between melt-pool dimensions gathered from experiments and simulation results.

laser power [W]	scan speed [mm/s]	layer thick. [μm]	width exp. [μm]	width sim. [μm]	err. [%]	depth exp. [μm]	depth sim. [μm]	err. [%]
160	960	40	116 ± 2	122	+5.2	68 ± 2	74	+8.8
190	960	40	125 ± 4	128	+2.4	88 ± 4	81	-7.9
220	960	40	138 ± 3	144	+4.3	95 ± 2	89	-6.3

ing the layer thickness increases the unit powder volume that absorbs the energy, thereby slightly decreasing the maximum temperatures, that is in agreement with the previous studies [62]. In addition, increasing the hatch spacing from 75 μm to 100 μm had a negligible effect on the maximum temperatures. All four process parameters had different effect on the maximum temperatures. Laser power and scan speed had the most dominant effect on the maximum temperature.

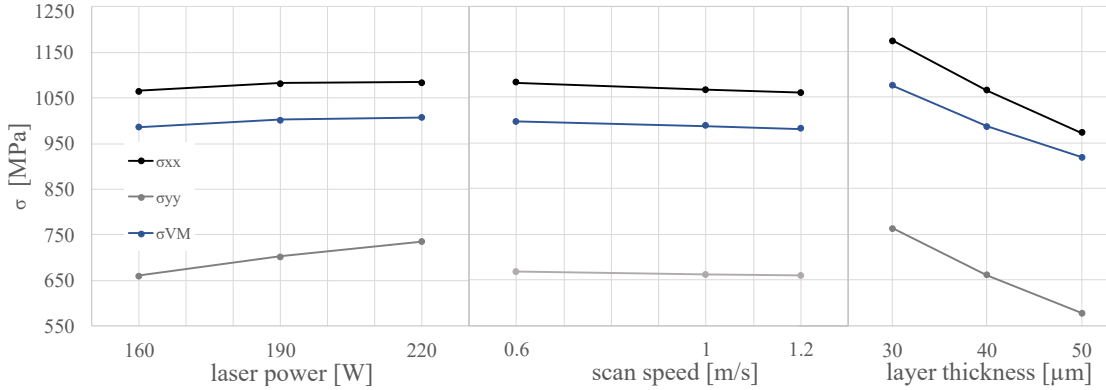


Figure 11: Effect of laser power, scan speed and layer thickness on average longitudinal, average transverse and average Von-Mises stresses after cooling down to ambient temperature.

Figure 11 shows the effect of process parameters on the average longitudinal and transverse normal stresses in the build layer after cooling down. The maximum value of the longitudinal stress was not affected by any of the process parameters and it was slightly above the yield strength of the material. Both the average longitudinal and transverse stresses were directly proportional to the layer thickness. This is attributed to the constant thermal load applied over a larger thickness, and thereby lowering the stresses with increasing layer thicknesses which has been also concluded in several studies [63, 29]. In addition, the average transverse stresses was directly proportional to the laser power and an inverse proportionality with the scan speed that is consistent with previous articles [64, 26]. However, the influence of scan speed on transverse stresses was not significant, which has been also confirmed by Shiomi et al. [28]. The hatch spacing did not have a considerable effect on stress. Residual stresses along the longitudinal direction were approximately 150% greater than the stresses along the transverse direction for all of the parameters which is in agreement with the similar experimental findings in literature [65, 30].

Figure 12 shows the effect of unidirectional and zigzag scan patterns on the resultant stress

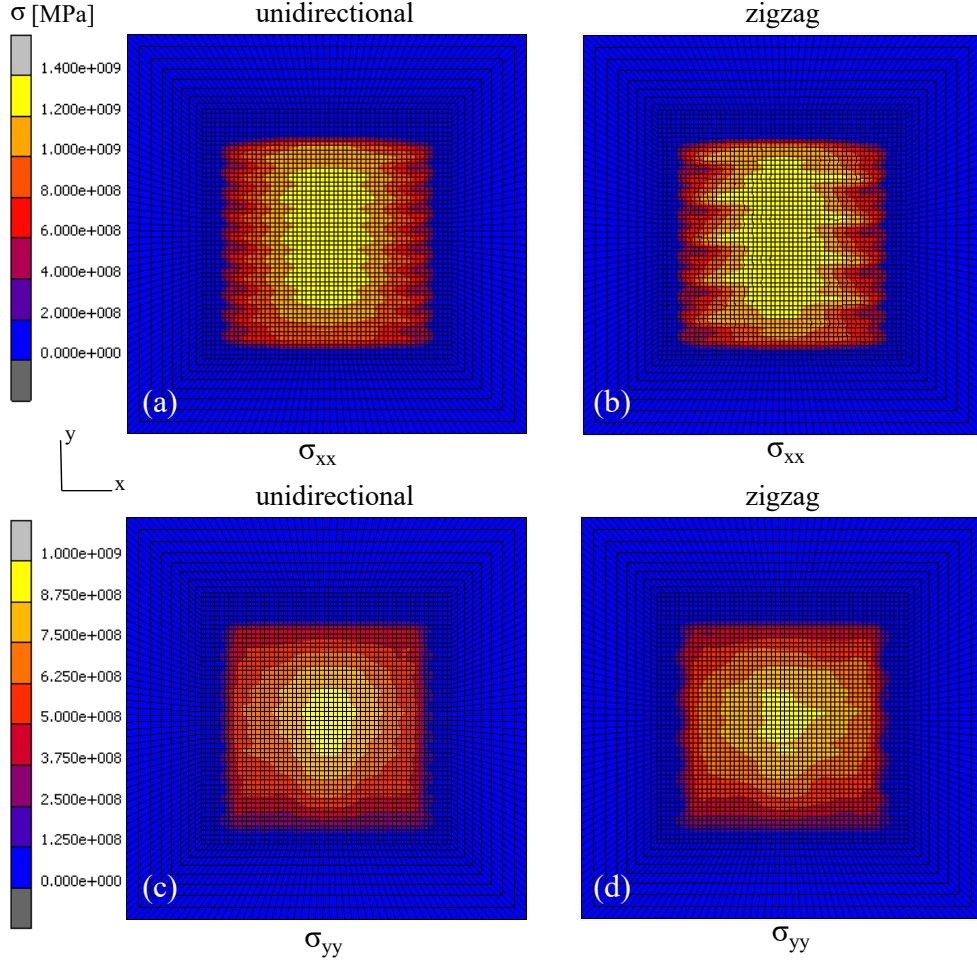


Figure 12: Thermomechanical simulation results for different scan patterns: **a.** σ_{xx} [MPa] for unidirectional, (a) σ_{xx} [MPa] for unidirectional, (b) σ_{xx} [MPa] for zigzag, (c) σ_{yy} [MPa] for unidirectional, and (d) σ_{yy} [MPa] for zigzag. $P = 160$ W, $v = 1000$ mm/s, $\Delta d = 90$ μ m, $\Delta h = 40$ μ m.

field using thermomechanical simulations. Both the average and maximum stresses for the two components were almost the same in terms of magnitude, while the stress solutions are slightly different. The temperature difference at the starting point of a track was much higher in comparison to the unidirectional pattern and hence causing higher thermal gradients and higher stresses. In contrast, each scan track starts near the end of the previously scanned track, thus causing less temperature differences between the two consecutive tracks for the zig-zag pattern. However, there is a longer distance travelled between the two starting points of consecutive tracks that led to a higher temperature gradient. Consequently, the stress distribution of zigzag showed a relatively higher alternating behavior with as can be observed in Figure 12(b). This result is in agreement with the findings of Parry et al. [32].

Figure 13 shows all six stress components at the end of the thermomechanical simulation after cooling down to baseplate temperature. Longitudinal and transverse stress components were dominant in terms of magnitudes in comparison to the others. The maximum of the normal stress along the build direction and shear stresses were at least and order of magnitude

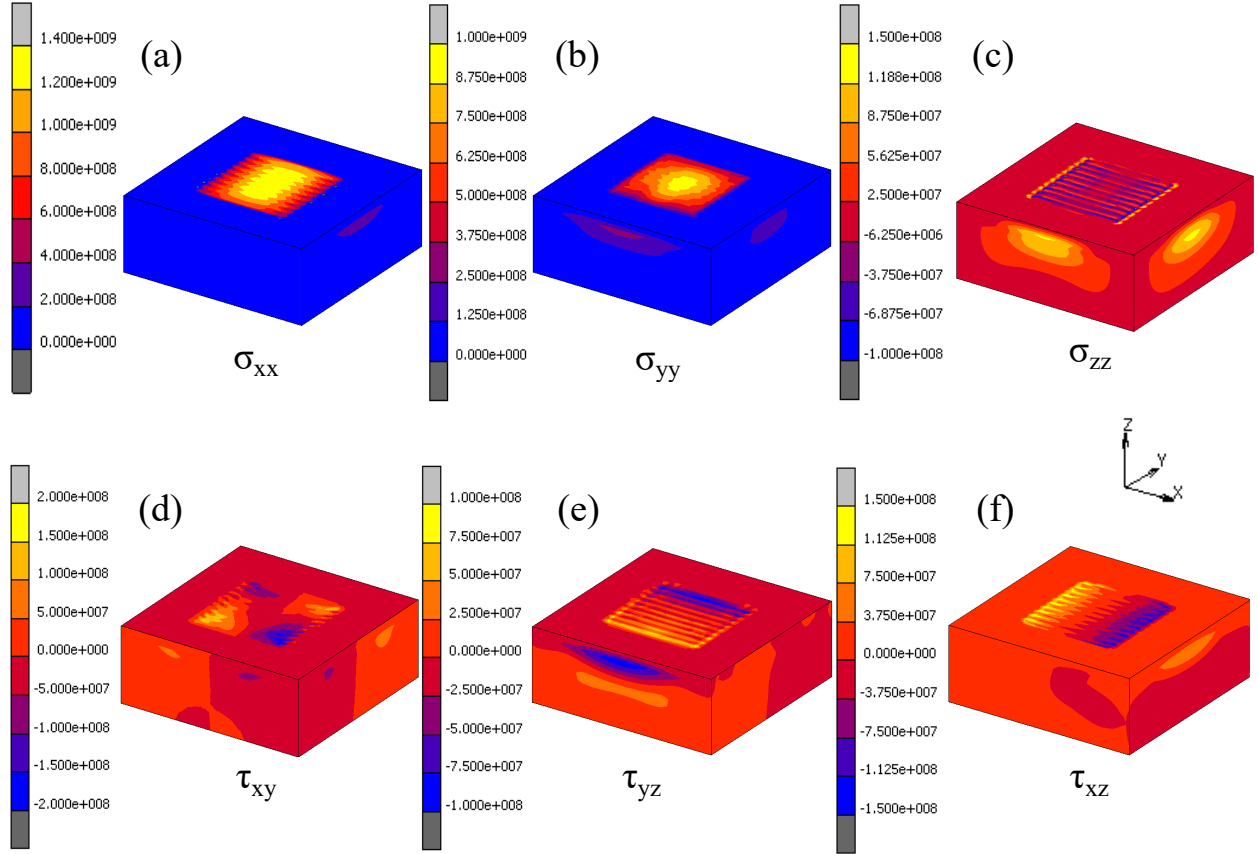


Figure 13: Stress distributions after cooling down of the a single layer. (a) σ_{xx} [MPa], (b) σ_{yy} [MPa], (c) σ_{zz} [MPa], (d) τ_{xy} [MPa], (e) τ_{yz} [MPa], (f) τ_{xz} [MPa]. $P = 160$ W, $v = 1000$ mm/s, $\Delta d = 90$ μ m, $\Delta h = 40$ μ m, and unidirectional scan pattern.

lower than the in-plane stresses. The corners at the boundaries of the deposition area act as stress concentrations, hence local stresses were greater in those regions. The powder region, on the other hand, had relatively low stresses. Since the powder had a very low elastic modulus (approximately 0.1 GPa), elements at powder state experiences large deformations with a relatively lower stresses.

Figure 14 shows distributions of longitudinal and transverse stresses of the thermomechanical and ISM solutions. These figures show the stresses after the cool down of build layer to a steady-state base-plate temperature completely. The process parameters were 160 W, 1000 mm/s, 90 μ m, and 40 μ m for laser power, scan speed, hatch spacing, and layer thickness, respectively. The distributions of both longitudinal and transverse stresses of the ISM results were consistent with those of the thermomechanical solution. The region that had the largest longitudinal stresses for the ISM results were slightly greater than that for the thermomechanical solution. Besides, the maximum magnitude of the transverse stresses was slightly over-predicted for the ISM method in comparison to that for the thermomechanical solution. The computational time was reduced by approximately six times in comparison to the thermomechanical solution.

Table 5 presents a comparison of the simulation results of the ISM and thermomechanical

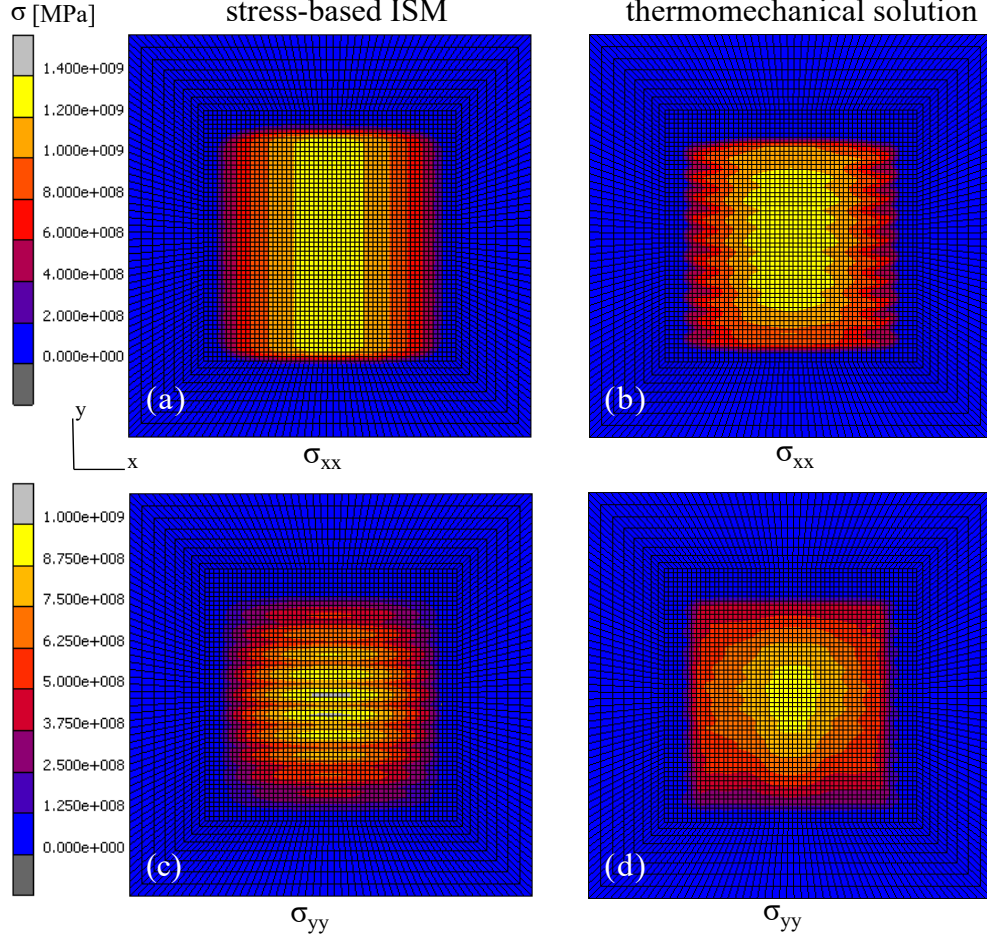


Figure 14: Results of stress components for different methods: (a) σ_{xx} [MPa] of ISM, (b) σ_{xx} [MPa] of thermomechanical solution, (c) σ_{yy} [MPa] of ISM, and (d) σ_{yy} [MPa] of thermomechanical solution. $P = 160$ W, $v = 1000$ mm/s, $\Delta d = 90$ μ m, $\Delta h = 40$ μ m.

solution for different process parameters. The stress values were obtained by taking the average values over the surface of the deposited region/area. The resulting distributions showed the negligible effect of the process parameters on the average of longitudinal stress component. On the contrary, the ISM successfully predicts longitudinal stress distributions with a reasonable accuracy. ISM predicted stresses within approximately 15% variation with respect to the thermomechanical results by using only the maximum temperature information. The only exceptional parameter was the layer thickness, which had the largest mismatch between longitudinal and transverse stresses of 13.2% and 15.1%, respectively. This is actually an expected result since ISM does not take into account the layer thickness. The volume of the domain changes with varying layer thickness. But the thermal loads remain the same for the same power and scan speed. Stress as being force over a unit area becomes inversely proportional to the layer thickness which was consistent with the findings in the literature [63, 29]. The ISM shall further be improved by using a correction factor to account for the layer thickness.

Figure 15 shows the comparison of the current numerical to simulation and experimental

Table 5: Comparison between average stresses computed by thermomechanical solution and ISM results.

laser power [W]	scan speed [mm/s]	hatch spacing [μm]	layer thick. [μm]	Thermo mechanical σ_{xx} [MPa]	IS method σ_{xx} [MPa]	err. [%]	Thermo, mechanical σ_{yy} [MPa]	IS method σ_{yy} [MPa]	err. [%]
160	1000	90	40	1085	1100	+1.4	661	654	-1.1
190	1000	90	40	1082	1100	+1.7	703	704	+0.1
220	1000	90	40	1066	1100	+3.2	736	733	-0.4
160	600	90	40	1082	1100	+1.7	669	717	+7.2
160	1200	90	40	1060	1100	+3.8	658	632	-4.0
160	1000	75	40	1082	1100	+1.7	660	671	+1.7
160	1000	100	40	1080	1100	+1.9	689	635	-7.8
160	1000	90	30	1174	1100	-6.3	763	651	-14.7
160	1000	90	50	972	1100	+13.2	578	665	+15.1
260	1500	90	40	1103	1100	-0.3	788	718	-8.9

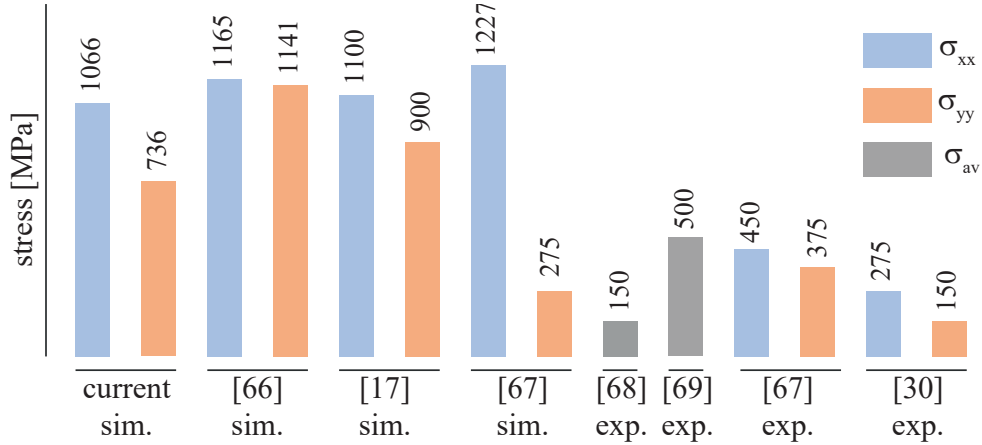


Figure 15: Comparison of residual stress result with various simulation (sim.) and experimental (exp.) findings from literature for IN718.

findings in the literature for IN718. The average stresses were compared only to be able compare to the simulation findings in the literature. However, the stresses are over predicted by the simulations in comparison the experiments. The model needs further improvement such as incorporation of latent heat effect to reduce the maximum temperatures hence stresses.

Simulation findings of Cheng et al. [66] for line scan pattern reveals average longitudinal stress magnitude that was close to the current study. Similarly, the numerical study of Denlinger et al. captured approximately the same trends as in the current study for the average of the longitudinal stress component [17]. However, in both references the transverse stresses were over predicted in comparison the current study. On the other hand, Chen et al. predicted a lower average for the transverse stress component [67]. The experimental works were obtained using an average over a large build region that was necessary to carry out experimental stress measurements. For this reason, the experimental stresses were significantly lower than the theoretically predicted stresses. In references [68] and [69], the direction of

the measured stress component were not indicated besides, the stresses were obtained by averaging over the build region for comparison. In the reference [67], although the effect of overlap was investigated, it is possible to conclude from the unidirectional patterns where the stresses reach to a steady-state magnitude. Accordingly the experimental stress results for the long line builds that were obtained by contouring method were provided for comparison [30]. In general, the averaging of the experimental results revealed lower stress magnitudes than the numerical predictions although the simulations were consistent with the similar studies in the literature.

Thermomechanical process simulations have numerical challenges due to the existence of high temperature gradients leading to large thermal strains and translations between the very soft powder and the other states. Therefore, the ISM provides an easy alternative to find the stresses directly from a thermal solution. However, ISM method fails to correlate to layer thickness. In addition, further studies are necessary to check its effectiveness in multiple layer simulations, and its predictive capability at part scale through part scale experimental measurements.

6. Conclusions

In this study, a numerical methodology was developed in a commercial FE environment with user-subroutines to simulate thermomechanical LPBF process with temperature-and state-dependent properties. In addition, an inherent strain method was implemented and its comparison to the thermomechanical model reveals the following important conclusions:

- The thermomechanical model predicts experimental melt-pool dimensions accurately, by considering the temperature and state-dependent material properties.
- Expression of surface heat losses in terms of a volumetric heat loss terms simplifies the need for a definition of free surfaces and their update after deposition of each layer.
- The process parameters do not significantly change the residual stresses along the scanning direction which are close to the yield stress.
- The ISM revealed nearly six times faster solution than that of the thermomechanical approach within approximately 10% accuracy.
- Thermomechanical model reveals residual stresses that are inversely proportional to layer thickness. The ISM procedure needs further improvement to consider the effect of layer thickness.
- In this study latent heat effect is not considered that has led to the over prediction of temperatures and stresses. It is essential to incorporate latent heat effect for more accurate temperature and stress predictions.

The proposed ISM method will be further improved to perform multi-layer simulations, to consider of stress relaxation effects in order to predict distortions and residual stresses at part scale accurately and precisely.

7. Acknowledgement

We greatly acknowledge the scholarship awarded by Sabanci University - Faculty of Natural Sciences and Engineering, which is used to fund the graduate student (C.B.) to perform the research activities in this study. We thank M.Sc. Kerem Dortkasli at Sabanci University and Dr. Kemal Davut at Izmir Institute of Technology for the electron microscopy images.

Appendix A. Material properties

Table A.1: Constant properties of stainless steel (SS316) baseplate material (SS316) [70].

ρ [kg/m ³]	C_p [J/K/kg]	k_s [W/m/kg]	α [K ⁻⁵]	E [GPa]	σ_y [MPa]	ν
7700	450	14	1.17	198.5	282	0.3

Table A.2: Evaporation heat loss constants in Eq. (7).

ΔH_ν^* [J/g]	M [g/mol]	R [J/mol/K]	T_ν [K]	P_0 [Pa]
6.4×10^3	59.75	8.314	3188	101325

Note that the latent heat effect, that causes a jump in the heat capacitance at the solid to liquid transition state, can be incorporated to the heat capacitance as in the references [55].

References

- [1] M. K. Thompson, G. Moroni, T. Vaneker, G. Fadel, R. I. Campbell, I. Gibson, A. Bernard, J. Schulz, P. Graf, B. Ahuja, et al., Design for additive manufacturing: Trends, opportunities, considerations, and constraints, CIRP annals 65 (2) (2016) 737–760.
- [2] J.-P. Kruth, M.-C. Leu, T. Nakagawa, Progress in additive manufacturing and rapid prototyping, CIRP Annals-Manufacturing Technology 47 (2) (1998) 525–540.
- [3] T. DebRoy, H. Wei, J. Zuback, T. Mukherjee, J. Elmer, J. Milewski, A. M. Beese, A. Wilson-Heid, A. De, W. Zhang, Additive manufacturing of metallic components—process, structure and properties, Progress in Materials Science 92 (2018) 112–224.
- [4] D. Bourell, J. P. Kruth, M. Leu, G. Levy, D. Rosen, A. M. Beese, A. Clare, Materials for additive manufacturing, CIRP Annals 66 (2) (2017) 659–681.
- [5] C. Lindemann, U. Jahnke, M. Moi, R. Koch, Analyzing product lifecycle costs for a better understanding of cost drivers in additive manufacturing, in: 23th Annual International Solid Freeform Fabrication Symposium—An Additive Manufacturing Conference. Austin Texas USA 6th-8th August, 2012.

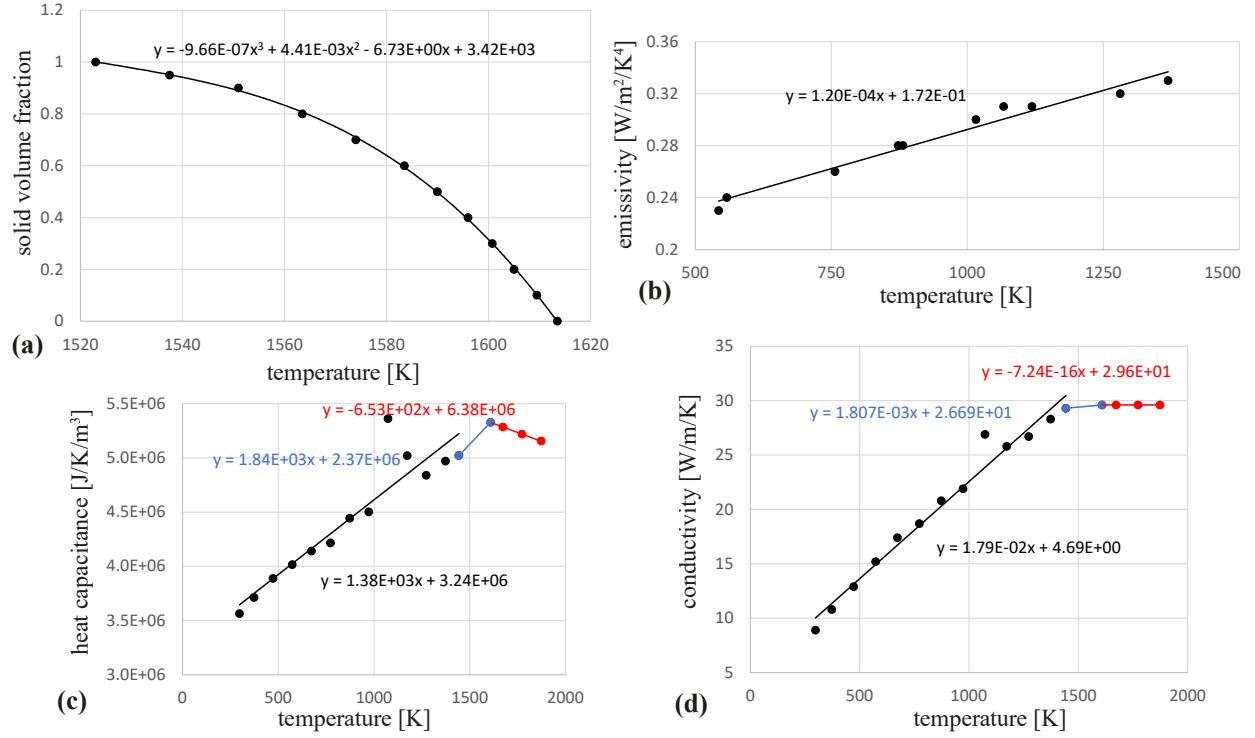


Figure A.1: Temperature dependent thermal properties of IN718 [71]: (a) solid volume fraction, $f^{(s)}$, (b) emissivity, ϵ , (c) heat capacitance, ρC_p , and (d) thermal conductivity, k . The black, blue, and red lines indicate the different fits for solid, mushy, and liquid states.

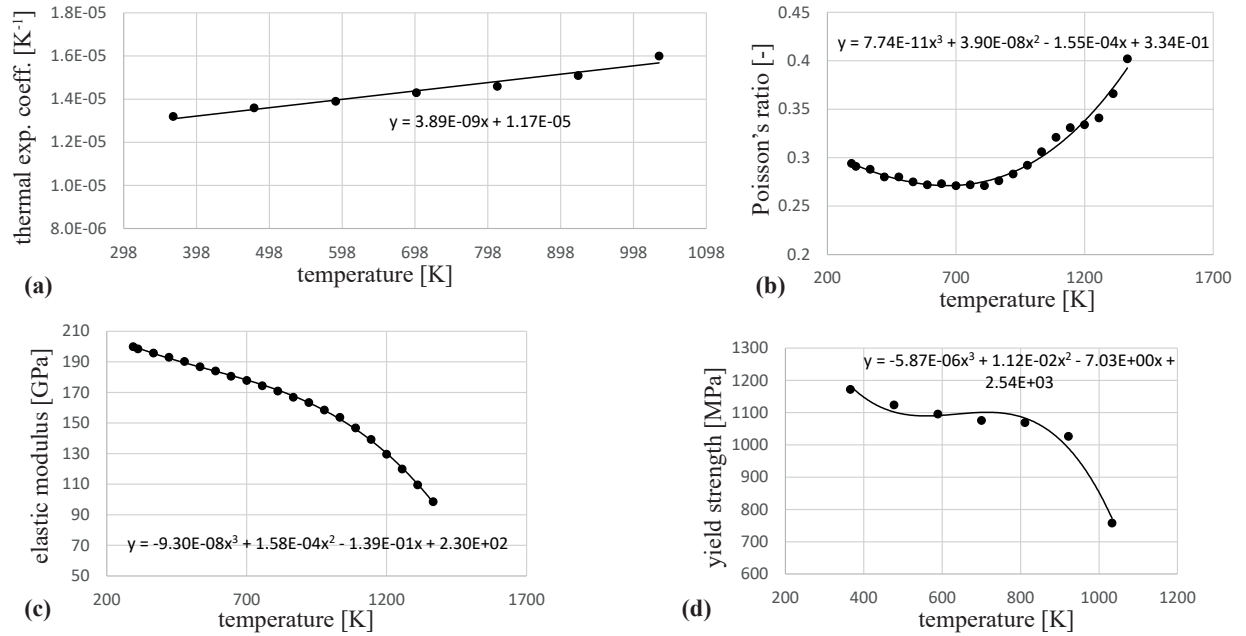


Figure A.2: Temperature-dependent mechanical properties of IN718 [72]: (a) thermal expansion coefficient, α , (b) Poisson's ratio, ν , (c) elastic modulus, E , and (d) yield strength, σ_y .

- [6] M. Galati, L. Iuliano, A literature review of powder-based electron beam melting focusing on numerical simulations, *Additive Manufacturing* 19 (2018) 1–20.
- [7] J. Smith, W. Xiong, W. Yan, S. Lin, P. Cheng, O. L. Kafka, G. J. Wagner, J. Cao, W. K. Liu, Linking process, structure, property, and performance for metal-based additive manufacturing: computational approaches with experimental support, *Computational Mechanics* 57 (4) (2016) 583–610.
- [8] M. M. Francois, A. Sun, W. E. King, N. J. Henson, D. Turret, C. A. Bronkhorst, N. N. Carlson, C. K. Newman, T. S. Haut, J. Bakosi, et al., Modeling of additive manufacturing processes for metals: Challenges and opportunities, *Current Opinion in Solid State and Materials Science* 21 (LA-UR-16-24513; SAND-2017-6832J) (2017).
- [9] W. King, A. T. Anderson, R. M. Ferencz, N. E. Hodge, C. Kamath, S. A. Khairallah, Overview of modelling and simulation of metal powder bed fusion process at lawrence livermore national laboratory, *Materials Science and Technology* 31 (8) (2015) 957–968.
- [10] A. Bauereiß, T. Scharowsky, C. Körner, Defect generation and propagation mechanism during additive manufacturing by selective beam melting, *Journal of Materials Processing Technology* 214 (11) (2014) 2522–2528.
- [11] L.-E. Lindgren, A. Lundbäck, M. Fisk, R. Pederson, J. Andersson, Simulation of additive manufacturing using coupled constitutive and microstructure models, *Additive Manufacturing* 12 (2016) 144–158.
- [12] J. Liu, B. Jalalahmadi, Y. Guo, M. P. Sealy, N. Bolander, A review of computational modeling in powder-based additive manufacturing for metallic part qualification, *Rapid Prototyping Journal* (2018).
- [13] B. Schoinochoritis, D. Chantzis, K. Salonitis, Simulation of metallic powder bed additive manufacturing processes with the finite element method: A critical review, *Proceedings of the Institution of Mechanical Engineers, Part B: Journal of Engineering Manufacture* 231 (1) (2017) 96–117.
- [14] Z. Luo, Y. Zhao, A survey of finite element analysis of temperature and thermal stress fields in powder bed fusion additive manufacturing, *Additive Manufacturing* 21 (2018) 318–332.
- [15] N. W. Klingbeil, J. L. Beuth, R. Chin, C. Amon, Residual stress-induced warping in direct metal solid freeform fabrication, *International Journal of Mechanical Sciences* 44 (1) (2002) 57–77.
- [16] I. A. Roberts, C. Wang, R. Esterlein, M. Stanford, D. Mynors, A three-dimensional finite element analysis of the temperature field during laser melting of metal powders in additive layer manufacturing, *International Journal of Machine Tools and Manufacture* 49 (12-13) (2009) 916–923.

- [17] E. R. Denlinger, M. Gouge, J. Irwin, P. Michaleris, Thermomechanical model development and in situ experimental validation of the laser powder-bed fusion process, *Additive Manufacturing* 16 (2017) 73–80.
- [18] M. Chiumenti, E. Neiva, E. Salsi, M. Cervera, S. Badia, J. Moya, Z. Chen, C. Lee, C. Davies, Numerical modelling and experimental validation in selective laser melting, *Additive Manufacturing* 18 (2017) 171–185.
- [19] P. Michaleris, Modeling metal deposition in heat transfer analyses of additive manufacturing processes, *Finite Elements in Analysis and Design* 86 (2014) 51–60. doi:10.1016/j.finel.2014.04.003.
- [20] R. Andreotta, L. Ladani, W. Brindley, Finite element simulation of laser additive melting and solidification of inconel 718 with experimentally tested thermal properties, *Finite Elements in Analysis and Design* 135 (2017) 36–43.
- [21] C. Fu, Y. Guo, Three-dimensional temperature gradient mechanism in selective laser melting of ti-6al-4v, *Journal of Manufacturing Science and Engineering* 136 (6) (2014).
- [22] B. Schoinochoritis, D. Chantzis, K. Salonitis, Simulation of metallic powder bed additive manufacturing processes with the finite element method: A critical review, *Proceedings of the Institution of Mechanical Engineers, Part B: Journal of Engineering Manufacture* 231 (1) (2017) 96–117. doi:10.1177/0954405414567522.
- [23] L. Scime, J. Beuth, Melt pool geometry and morphology variability for the Inconel 718 alloy in a laser powder bed fusion additive manufacturing process, *Additive Manufacturing* 29 (August) (2019) 100830. doi:10.1016/j.addma.2019.100830.
- [24] T. Mukherjee, W. Zhang, T. DebRoy, An improved prediction of residual stresses and distortion in additive manufacturing, *Computational Materials Science* 126 (2017). doi:10.1016/j.commatsci.2016.10.003.
- [25] B. Vrancken, R. Wauthle, J. P. Kruth, J. Van Humbeeck, Study of the influence of material properties on residual stress in selective laser melting, *24th International SFF Symposium - An Additive Manufacturing Conference, SFF 2013* (2013) 393–407.
- [26] T. Simson, A. Emmel, A. Dwars, J. Böhm, Residual stress measurements on aisi 316l samples manufactured by selective laser melting, *Additive Manufacturing* 17 (2017) 183–189.
- [27] J. L. Bartlett, X. Li, An overview of residual stresses in metal powder bed fusion, *Additive Manufacturing* 27 (January) (2019) 131–149. doi:10.1016/j.addma.2019.02.020.
- [28] M. Shiomi, K. Osakada, K. Nakamura, T. Yamashita, F. Abe, Residual stress within metallic model made by selective laser melting process, *CIRP Annals - Manufacturing Technology* 53 (1) (2004) 195–198. doi:10.1016/S0007-8506(07)60677-5.

- [29] L. S. Anderson, A. M. Venter, B. Vrancken, D. Marais, J. V. Humbeeck, Investigating the Residual Stress Distribution in Selective Laser Melting Produced Ti-6Al-4V using Neutron Diffraction, Mechanical Stress Evaluation by Neutron and Synchrotron Radiation 4 (2018) 73–78. doi:10.21741/9781945291678-11.
- [30] J. Robinson, I. Ashton, P. Fox, E. Jones, C. Sutcliffe, Determination of the effect of scan strategy on residual stress in laser powder bed fusion additive manufacturing, Additive Manufacturing 23 (2018) 13–24.
- [31] E. GmbH, Corporate website, accessed: 17.05.2020 (2020).
URL <http://www.eos.info/en>
- [32] L. Parry, I. Ashcroft, R. D. Wildman, Understanding the effect of laser scan strategy on residual stress in selective laser melting through thermo-mechanical simulation, Additive Manufacturing 12 (2016) 1–15.
- [33] S. D. Bagg, L. M. Sochalski-Kolbus, J. R. Bunn, The effect of laser scan strategy on distortion and residual stresses of arches made with selective laser melting (2016).
- [34] C. Li, J. Liu, Y. Guo, Efficient multiscale prediction of cantilever distortion by selective laser melting, in: Proceedings of the 27th Annual International Solid Freeform Fabrication Symposium, 2016, pp. 236–246.
- [35] S. Afazov, W. A. Denmark, B. L. Toralles, A. Holloway, A. Yaghi, Distortion prediction and compensation in selective laser melting, Additive Manufacturing 17 (2017) 15–22.
- [36] N. Patil, D. Pal, B. Stucker, et al., A new finite element solver using numerical eigen modes for fast simulation of additive manufacturing processes, in: Proceedings of the Solid Freeform Fabrication Symposium, 2013, pp. 12–14.
- [37] Y. Zhang, G. Guillemot, M. Bernacki, M. Bellet, Macroscopic thermal finite element modeling of additive metal manufacturing by selective laser melting process, Computer Methods in Applied Mechanics and Engineering 331 (2018) 514–535.
- [38] R. J. Williams, C. M. Davies, P. A. Hooper, A pragmatic part scale model for residual stress and distortion prediction in powder bed fusion, Additive Manufacturing 22 (2018) 416–425.
- [39] R. K. Ganeriwala, N. E. Hodge, J. M. Solberg, Towards improved speed and accuracy of laser powder bed fusion simulations via multiscale spatial representations, Computational Materials Science 187 (2021) 110112.
- [40] E. Neiva, M. Chiumenti, M. Cervera, E. Salsi, G. Piscopo, S. Badia, A. F. Martín, Z. Chen, C. Lee, C. Davies, Numerical modelling of heat transfer and experimental validation in powder-bed fusion with the virtual domain approximation, Finite Elements in Analysis and Design 168 (2020) 103343.

- [41] Y. Luo, H. Murakawa, Y. Ueda, Prediction of welding deformation and residual stress by elastic fem based on inherent strain (report i): mechanism of inherent strain production (mechanics, strength & structure design), Transactions of JWRI 26 (2) (1997) 49–57.
- [42] D. Camilleri, T. Comlekci, T. F. Gray, Computational prediction of out-of-plane welding distortion and experimental investigation, The Journal of Strain Analysis for Engineering Design 40 (2) (2005) 161–176.
- [43] A. M. Korsunsky, G. M. Regino, D. Nowell, Variational eigenstrain analysis of residual stresses in a welded plate, International Journal of Solids and Structures 44 (13) (2007) 4574–4591.
- [44] T.-S. Jun, A. M. Korsunsky, Evaluation of residual stresses and strains using the eigenstrain reconstruction method, International Journal of Solids and Structures 47 (13) (2010) 1678–1686.
- [45] J. Ding, P. Colegrove, J. Mehnen, S. Ganguly, P. S. Almeida, F. Wang, S. Williams, Thermo-mechanical analysis of wire and arc additive layer manufacturing process on large multi-layer parts, Computational Materials Science 50 (12) (2011) 3315–3322.
- [46] L. Cheng, A. To, Part-scale build orientation optimization for minimizing residual stress and support volume for metal additive manufacturing: Theory and experimental validation, Computer-Aided Design 113 (2019) 1–23.
- [47] P. Promoppatum, V. Uthaisangsuk, Part scale estimation of residual stress development in laser powder bed fusion additive manufacturing of Inconel 718, Finite Elements in Analysis and Design 189 (January) (2021) 103528. doi:10.1016/j.finel.2021.103528.
- [48] M. Bugatti, Q. Semeraro, Limitations of the inherent strain method in simulating powder bed fusion processes, Additive Manufacturing 23 (2018) 329–346.
- [49] X. Liang, L. Cheng, Q. Chen, Q. Yang, A. C. To, A modified method for estimating inherent strains from detailed process simulation for fast residual distortion prediction of single-walled structures fabricated by directed energy deposition, Additive Manufacturing 23 (2018) 471–486.
- [50] Y. Lee, W. Zhang, Modeling of heat transfer, fluid flow and solidification microstructure of nickel-base superalloy fabricated by laser powder bed fusion, Additive Manufacturing 12 (2016) 178–188.
- [51] M. Marc, Volume a: Theory and user information, MSC. Software Corporation (2010).
- [52] R. D. Cook, et al., Concepts and applications of finite element analysis, John wiley & sons, 2007.
- [53] Y.-c. Fung, P. Tong, X. Chen, Classical and computational solid mechanics, Vol. 2, World Scientific Publishing Company, 2017.

- [54] X. Zhao, A. Iyer, P. Promoppatum, S.-C. Yao, Numerical modeling of the thermal behavior and residual stress in the direct metal laser sintering process of titanium alloy products, *Additive Manufacturing* 14 (2017) 126–136.
- [55] P. Promoppatum, V. Uthaisangsuk, Part scale estimation of residual stress development in laser powder bed fusion additive manufacturing of inconel 718, *Finite Elements in Analysis and Design* 189 (2021) 103528.
- [56] G. R. Hadley, Thermal conductivity of packed metal powders, *International Journal of Heat and Mass Transfer* 29 (6) (1986) 909–920.
- [57] Y. Zhang, G. Guillemot, M. Bernacki, M. Bellet, Macroscopic thermal finite element modeling of additive metal manufacturing by selective laser melting process, *Computer Methods in Applied Mechanics and Engineering* 331 (2018) 514–535. doi:10.1016/j.cma.2017.12.003.
- [58] Q. Chen, X. Liang, D. Hayduke, J. Liu, L. Cheng, J. Oskin, R. Whitmore, A. C. To, An inherent strain based multiscale modeling framework for simulating part-scale residual deformation for direct metal laser sintering, *Additive Manufacturing* 28 (2019) 406–418.
- [59] Z. Zhang, Y. Huang, A. Rani Kasinathan, S. Imani Shahabad, U. Ali, Y. Mahmoodkhani, E. Toyserkani, 3-Dimensional heat transfer modeling for laser powder-bed fusion additive manufacturing with volumetric heat sources based on varied thermal conductivity and absorptivity, *Optics and Laser Technology* 109 (July 2018) (2019) 297–312. doi:10.1016/j.optlastec.2018.08.012.
- [60] V. Popovich, E. Borisov, A. Popovich, V. S. Sufiarov, D. Masaylo, L. Alzina, Functionally graded inconel 718 processed by additive manufacturing: Crystallographic texture, anisotropy of microstructure and mechanical properties, *Materials & Design* 114 (2017) 441–449.
- [61] B. K. Panda, S. Sahoo, Thermo-mechanical modeling and validation of stress field during laser powder bed fusion of alsi10mg built part, *Results in Physics* 12 (2019) 1372–1381. doi:https://doi.org/10.1016/j.rinp.2019.01.002.
- [62] M. F. Zaeh, G. Branner, Investigations on residual stresses and deformations in selective laser melting, *Production Engineering* 4 (1) (2010) 35–45. doi:10.1007/s11740-009-0192-y.
- [63] L. Van Belle, G. Vansteenkiste, J. C. Boyer, Investigation of residual stresses induced during the selective laser melting process, in: *Key Engineering Materials*, Vol. 554, Trans Tech Publ, 2013, pp. 1828–1834.
- [64] G. Vastola, G. Zhang, Q. X. Pei, Y. W. Zhang, Controlling of residual stress in additive manufacturing of Ti6Al4V by finite element modeling, *Additive Manufacturing* 12 (2016) 231–239. doi:10.1016/j.addma.2016.05.010.

- [65] A. V. Gusarov, M. Pavlov, I. Smurov, Residual stresses at laser surface remelting and additive manufacturing, *Physics Procedia* 12 (PART 1) (2011) 248–254. doi:10.1016/j.phpro.2011.03.032.
- [66] B. Cheng, S. Shrestha, K. Chou, Stress and deformation evaluations of scanning strategy effect in selective laser melting, *Additive Manufacturing* 12 (2016) 240–251.
- [67] C. Chen, J. Yin, H. Zhu, Z. Xiao, L. Zhang, X. Zeng, Effect of overlap rate and pattern on residual stress in selective laser melting, *International Journal of Machine Tools and Manufacture* 145 (2019) 103433.
- [68] Y. Lu, S. Wu, Y. Gan, T. Huang, C. Yang, L. Junjie, J. Lin, Study on the microstructure, mechanical property and residual stress of slm inconel-718 alloy manufactured by differing island scanning strategy, *Optics & Laser Technology* 75 (2015) 197–206.
- [69] J. L. Bartlett, X. Li, An overview of residual stresses in metal powder bed fusion, *Additive Manufacturing* 27 (2019) 131–149.
- [70] D. Deng, S. Kiyoshima, Numerical simulation of residual stresses induced by laser beam welding in a SUS316 stainless steel pipe with considering initial residual stress influences, *Nuclear Engineering and Design* 240 (4) (2010) 688–696. doi:10.1016/j.nucengdes.2009.11.049.
- [71] K. C. Mills, Recommended values of thermophysical properties for selected commercial alloys, Woodhead Publishing, 2002.
- [72] H. T. Metals, accessed: 01.09.2021 (2015). [link].
URL <http://www.hightempmetals.com/techdata/hitempInconel718data.php>